

École doctorale n° 364 : Sciences Fondamentales et Appliquées

Doctorat ParisTech

T H È S E

pour obtenir le grade de docteur délivré par

l'École Nationale Supérieure des Mines de Paris

Spécialité doctorale "Science et Génie des Matériaux"

présentée et soutenue publiquement par

Ali SAAD

le DAY MONTH 2015

NUMERICAL MODELLING OF MACROSEGREGATION FORMED DURING SOLIDIFICATION WITH SHRINKAGE USING A LEVEL SET APPROACH

Directeurs de thèse: **Michel BELLET**
Charles-André GANDIN

Jury

M. jury 1,	affiliation	Rapporteur
M. jury 2,	affiliation	Rapporteur
M. jury 3,	affiliation	Examineur
M. jury 4,	affiliation	Examineur
M. jury 5,	affiliation	Examineur

MINES ParisTech

Centre de Mise en Forme des Matériaux (CEMEF)
UMR CNRS 7635, F-06904 Sophia Antipolis, France

Acknowledgement

Dedicated to humanity ...

Contents

1	General Introduction	1
1.1	Solidification notions	2
1.1.1	Solute partitioning	2
1.1.2	Dendritic growth	4
1.1.3	Mush permeability	6
1.2	Macrosegregation	7
1.2.1	Liquid thermosolutal convection	8
1.2.2	Solidification shrinkage	9
1.2.3	Movement of equiaxed grains	9
1.2.4	Solid deformation	9
1.3	Other defects	9
1.4	Industrial Worries	11
1.5	Project context and objectives	12
1.5.1	Context	12
1.5.2	Ojectives and outline	14
2	Modelling Review	19
2.1	Modelling macrosegregation	20
2.1.1	Macroscopic solidification model: monodomain	21
2.2	Eulerian and Lagrangian motion description	28
2.2.1	Overview	28
2.2.2	Interface capturing	30
2.3	Solidification models with level set	30
2.4	The level set method	31
2.4.1	Diffuse interface	31
2.4.2	Mixing Laws	33
2.5	Interface motion	36
2.5.1	Level set transport	36

Contents

2.5.2	Level set regularisation	37
2.6	Mesh adaptation	41
2.6.1	Metrics and anisotropy	41
2.6.2	<i>Remesh2</i> : Interface remeshing	43
2.6.3	<i>Remesh4</i> : Multi-criteria remeshing	44
3	Energy balance with thermodynamic tabulations	47
3.1	State of the art	48
3.2	Thermodynamic considerations	49
3.2.1	Volume averaging	49
3.2.2	The temperature-enthalpy relationship	50
3.2.3	Tabulation of properties	50
3.3	Numerical method	52
3.3.1	Enthalpy-based approach	56
3.3.2	Temperature-based approach	56
3.3.3	Convergence	57
3.4	Validation	58
3.5	Application: multicomponent alloy solidification	61
3.5.1	Tabulations	63
3.5.2	Discussion	65
3.6	Limitations	70
4	Macrosegregation with liquid metal motion	73
4.1	Introduction	75
4.2	Formulation stability	75
4.2.1	Stable mixed finite elements	76
4.2.2	Variational multiscale (VMS)	76
4.3	Navier-Stokes solver	77
4.3.1	Strong and weak formulations	77
4.3.2	Stabilisation parameters	81
4.3.3	Implementation	82
4.4	Application to multicomponent alloys	83
4.4.1	<i>Tsolver</i> validation with fluid flow	83
4.4.2	Results	86
4.5	Macroscopic prediction of channel segregates	92
4.5.1	Introduction	92
4.5.2	Experimental work	93
4.5.3	Macroscopic scale simulations	93

4.6	Meso-Macro prediction of channel segregates	102
4.6.1	Numerical method	102
4.6.2	Configuration	103
4.6.3	Effect of vertical temperature gradient	107
4.6.4	Effect of cooling rate	109
4.6.5	Effect of lateral temperature gradient	111
4.6.6	Mono-grain freckles	112
5	Macrosegregation with solidification shrinkage	115
5.1	Solidification shrinkage	117
5.2	Choice of interface tracking	117
5.3	Multidomain formalism	119
5.3.1	Assumptions	120
5.4	FE partitioned model	121
5.4.1	In the metal	122
5.4.2	In the air	126
5.5	FE monolithic model	128
5.5.1	Monolithic equations	128
5.6	1D application: solidification with inverse segregation	133
5.6.1	Geometry and boundary conditions	133
5.6.2	Shrinkage without macrosegregation	133
5.6.3	Shrinkage with macrosegregation	143
5.7	2D application: controlled solidification benchmark	153
5.7.1	Boundary condition effect	153
5.7.2	Computational configuration	155
5.7.3	Results	156
5.8	3D application: reduced-gravity solidification	161
5.8.1	Previous work	161
5.8.2	Computational configuration	164
5.8.3	Texus binary alloy	171
5.8.4	Texus ternary and quaternary alloys	179
	Bibliography	185

Contents

List of Acronyms

Acronym	Standing for
ALE	Arbitrary Lagrangian-Eulerian
BTR	Brittle temperature range
CAFD	Cellular Automata Finite Difference
CAFE	Cellular Automata Finite Element
CBB	Circumventing Babuška-Brezzi
CCEMLCC	Chill Cooling for the Electro-Magnetic Levitator in relation with Continuous Casting of steel
CEMEF	Centre de Mise en Forme des Matériaux
CFL	Courant–Friedrichs–Lewy
C.FL	Computing and FLuids
CSF	Continuum Surface Force
DLR	Deutsches Zentrum für Luft- und Raumfahrt
DSPG	Darcy-Stabilising/Petrov-Galerkin
EML	Electromagnetic levitation
ESA	European Space Agency
FEM	Finite Element Method
FVM	Finite Volume Method
GMAW	Gas Metal Arc Welding
ISS	International Space Station
IWT	Institut für Werkstofftechnik
LHS	Left-hand side
LSIC	Least squares on incompressibility constraint
LSM	Level set method
MAC	Marker-and-cell
PF	Phase field
PSPG	Pressure-Stabilising/Petrov-Galerkin
RHS	Right-hand side
RUB	Ruhr Universität Bochum
RVE	Representative Elementary Volume
SBB	Satisfying Babuška-Brezzi
SUPG	Streamline-Upwind/Petrov-Galerkin
VMS	Variational MultiScale
VOF	Volume Of Fluid

Contents

Chapter 2

Modelling Review

Contents

2.1 Modelling macrosegregation	20
2.1.1 Macroscopic solidification model: monodomain	21
2.2 Eulerian and Lagrangian motion description	28
2.2.1 Overview	28
2.2.2 Interface capturing	30
2.3 Solidification models with level set	30
2.4 The level set method	31
2.4.1 Diffuse interface	31
2.4.2 Mixing Laws	33
2.5 Interface motion	36
2.5.1 Level set transport	36
2.5.2 Level set regularisation	37
2.6 Mesh adaptation	41
2.6.1 Metrics and anisotropy	41
2.6.2 <i>Remesh2</i> : Interface remeshing	43
2.6.3 <i>Remesh4</i> : Multi-criteria remeshing	44

2.1 Modelling macrosegregation

Microsegregation models

Solid formation depends greatly on the ability of chemical species to diffuse within each of the solid and liquid phases, but also across the solid-liquid interface. Furthermore, chemical diffusion like all other diffusional processes, is a time-dependent phenomenon. One can thus conclude that two factors influence the amount of solid formation: cooling rate and diffusion coefficients. However, convection and other mechanical mixing sources, homogenise the composition much faster than atomic diffusion. As such, *complete mixing* in the liquid is always an acceptable assumption, regardless of the solidification time. Thus, we speak of infinite diffusion in the liquid. Nevertheless, diffusion in the solid, also known as *back diffusion*, is the only transport mechanism with very low diffusion coefficients. Therefore, chemical species require a long time, i.e. low cooling rate, to completely diffuse within the solid. The difference in diffusional behaviour at the scale of a secondary dendrite arm, is summarised by two limiting segregation models of perfect equilibrium and nonequilibrium, which are the lever rule and Gulliver-Scheil models, respectively. Afterwards, models with finite back diffusion are presented.

Lever rule

The lever rule considers an ideal equilibrium in all phases, i.e. solidification is extremely slow, hence phase compositions are homogeneous ($w^{l*} = w^l$ and $w^{s*} = w^s$) at all times as a consequence of complete mixing. These compositions are given by:

$$w^l = w^{l*} = k^{-1}w^{s*} = k^{-1}w^s \quad (2.1)$$

$$w^s = w^{s*} = \frac{k w_0}{k f^s + (1 - f^s)} \quad (2.2)$$

At the end of solidification, the composition of the solid phase is equal to the nominal composition, $w^s = w_0$.

Gulliver-Scheil

The other limiting case is the absence of diffusion in the solid. That includes also the diffusion at the interface, so nothing diffuses in or out. The consequence is a steady increase of the homogeneous liquid composition while the solid composition remains non-uniform. Compared to a full equilibrium approach, higher fractions of liquid will remain. In eutectic systems, liquid may exist until eutectic composition is reached,

triggering a eutectic solidification. The phase compositions with this approach are given by:

$$w^l = w^{l*} = k^{-1}w^{s*} \quad (2.3)$$

$$w^{s*} = kw_0(1 - f^s)^{k-1} \quad (2.4)$$

Finite back diffusion

It has been concluded that the assumption of a negligible back diffusion overestimates the liquid composition and the resulting eutectic fraction. Therefore, many models studied the limited diffusion in the solid. One of the earliest models is the Brody-Flemings models [Khan et al. 2014] that is based on a differential solute balance equation for a parabolic growth rate, as follows:

$$w^l = w^{l*} = k^{-1}w^{s*} \quad (2.5)$$

$$w^{s*} = kw_0 [1 - (1 - 2\text{Fo}^s k) f^s]^{\frac{k-1}{1-2\text{Fo}^s k}} \quad (2.6)$$

where Fo^s is the dimensionless *Fourier number* for diffusion in the solid [Dantzig and Rappaz 2009]. It depends on the solid diffusion coefficient D^s , solidification time t_s and the secondary dendrite arm spacing, as follows:

$$\text{Fo}^s = \frac{D^s t_s}{(\lambda_2/2)^2} \quad (2.7)$$

Several other models were since suggested and used. The interested reader is referred to the following non exhaustive list of publications: Clyne and Kurz [1981], Kobayashi [1988], Ni and Beckermann [1991], Wang and Beckermann [1993], Combeau et al. [1996], Martorano et al. [2003], and Tournet and Gandin [2009]. It is noted that some of these publications consider also a finite diffusion in the liquid phase.

2.1.1 Macroscopic solidification model: monodomain

In this section, we will present the macroscopic conservations equations that enable us to predict macrosegregation in single multiphase metal system.

Volume averaging

It is crucial for a solidification model to represent phenomena on the microscale, then scale up to predict macroscopic phenomena. Nevertheless, the characteristic length of a small scale in solidification may represent a dendrite arm spacing, for instance

the mushy zone permeability, as it may also represent an atomic distance if one is interested, for instance, in the growth competition between diffusion and surface energy of the solid-liquid interface.

Modelling infinitely small-scale phenomena could be prohibitively expensive in computation time, if we target industrial scales. The volume averaging is a technique that allows bypassing this barrier by averaging small-scale variations on a so-called *representative volume element* (RVE) [Dantzig and Rappaz 2009] of volume V_E , with the following dimensional constraints: the element should be large enough to "see" and average microscopic fluctuations whilst being smaller than the scale of macroscopic variations.

Solid and liquid may exist simultaneously in the RVE, but no gas phase is considered (volume saturation: $V^s + V^l = V_E$). Moreover, temperature is assumed uniform and equal for all the phases. The formalism, introduced by Ni and Beckermann [1991], is summarised by the following equations for any physical quantity ψ :

$$\langle \psi \rangle = \frac{1}{V_E} \int_{V_E} \psi \, d\Omega = \langle \psi^s \rangle + \langle \psi^l \rangle \quad (2.8)$$

where $\langle \psi \rangle^s$ and $\langle \psi \rangle^l$ are phase averages of ψ . Then, for any phase ϕ , one can introduce the *phase intrinsic average* of ψ , denoted $\langle \psi \rangle^\phi$, by writing:

$$\langle \psi^\phi \rangle = \frac{1}{V_E} \int_{V_\phi} \psi \, d\Omega = g^\phi \langle \psi \rangle^\phi \quad (2.9)$$

where g^ϕ is the volume fraction of phase ϕ with $g^\phi = V_\phi/V_E$. To finalize, the averaging is applied to temporal and spatial derivation operators:

$$\left\langle \frac{\partial \psi^\phi}{\partial t} \right\rangle = \frac{\partial \langle \psi^\phi \rangle}{\partial t} - \int_{\Gamma^*} \psi^\phi \mathbf{v}^* \cdot \mathbf{n}^\phi \, dA \quad (2.10)$$

$$\langle \nabla \psi^\phi \rangle = \nabla \langle \psi^\phi \rangle + \int_{\Gamma^*} \psi^\phi \mathbf{n}^\phi \, dA \quad (2.11)$$

where \mathbf{v}^* is the local relative interface velocity and Γ^* is the solid-liquid interface, while \mathbf{n}^ϕ is the normal to Γ^* , directed outwards. The surface integral terms in eqs. (2.10) and (2.11) are *interfacial averages* that express exchanges between the phases across the interface.

The previous equations will be used to derive a set macroscopic conservation equations. It is noted that the intrinsic average $\langle \psi \rangle^\phi$ may be replaced by ψ^ϕ for notation simplicity, whenever the averaging technique applies.

Macroscopic equations

A monodomain macroscopic model relies on four main conservation equations to predict macrosegregation in a single alloy without any solidification shrinkage. It follows that no ambient gas will be taken into account. However, the conservation equations result are the result of all phases contributions in the alloy system. It is thus important to describe the general form of a phase-averaged conservation equation, for any physical quantity ψ :

$$\left\langle \frac{\partial \psi^\phi}{\partial t} \right\rangle + \left\langle \nabla \cdot \psi^\phi \mathbf{v}^\phi \right\rangle + \left\langle \nabla \cdot \mathbf{j}_{\psi^\phi} \right\rangle = \left\langle Q_{\psi^\phi} \right\rangle \quad (2.12)$$

The first LHS term in eq. (2.12) represents the time variation of ψ , the second term accounts for transport by advection while the third term accounts for diffusive transport of ψ , knowing its flux, \mathbf{j}_ψ . The RHS term represents a volumetric source. The considered equations are mass, energy, species conservation and momentum. The latter equation is averaged only for the liquid phase, as we assume a fixed and rigid solid phase ($\mathbf{v}^s = 0$), thus the corresponding equation vanishes.

We may then write each averaged macroscopic conservation equation as the sum of local conservation equations for each phase in the RVE. This will introduce the interfacial average terms defined earlier in eqs. (2.10) and (2.11). For instance, if we replace ψ by ρ for each phase $\phi \in \{l, s\}$, eq. (2.12) gives two phase-averaged mass balances, with interfacial terms:

$$\frac{\partial}{\partial t} (g^l \langle \rho \rangle^l) + \nabla \cdot (g^l \langle \rho \rangle^l \mathbf{v}^l) = S_V \langle \langle \rho \rangle^l \mathbf{v}^{l*} \cdot \mathbf{n} \rangle^* - S_V \langle \langle \rho \rangle^l \mathbf{v}^* \cdot \mathbf{n} \rangle^* \quad (2.13a)$$

$$\frac{\partial}{\partial t} (g^s \langle \rho \rangle^s) + \nabla \cdot (g^s \langle \rho \rangle^s \mathbf{v}^s) = -S_V \langle \langle \rho \rangle^s \mathbf{v}^{s*} \cdot \mathbf{n} \rangle^* + S_V \langle \langle \rho \rangle^s \mathbf{v}^* \cdot \mathbf{n} \rangle^* \quad (2.13b)$$

where $S_V = A_{sl}/V_E$ is the specific surface area, \mathbf{v}^{l*} and \mathbf{v}^{s*} are respectively, the liquid and solid phase velocity at the interface and \mathbf{v}^* is the previously introduced solid-liquid interface velocity. The $\langle \rangle^*$ notation in the RHS of eq. (2.13a) is expanded as follows [Dantzig and Rappaz 2009]:

$$S_V \langle \langle \rho \rangle^l \mathbf{v}^{l*} \cdot \mathbf{n} \rangle^* = \frac{A_{sl}}{V_E} \left(\frac{1}{A_{sl}} \int_{A_{sl}} \langle \rho \rangle^l \mathbf{v}^{l*} \cdot \mathbf{n} \, dA \right) \quad (2.14a)$$

$$= \frac{1}{V_E} \int_{A_{sl}} \langle \rho \rangle^l \mathbf{v}^{l*} \cdot \mathbf{n} \, dA \quad (2.14b)$$

Chapter 2. Modelling Review

Summing equations (2.13a) and (2.13b), results in the overall mass balance in the RVE:

$$\frac{\partial}{\partial t} \left(g^l \langle \rho \rangle^l + g^s \langle \rho \rangle^s \right) + \nabla \cdot \left(g^l \langle \rho \rangle^l \mathbf{v}^l + g^s \langle \rho \rangle^s \mathbf{v}^s \right) = S_V \left\langle \langle \rho \rangle^l \left(\mathbf{v}^{l*} - \mathbf{v}^* \right) \cdot \mathbf{n} \right\rangle^* - S_V \left\langle \langle \rho \rangle^s \left(\mathbf{v}^{s*} - \mathbf{v}^* \right) \cdot \mathbf{n} \right\rangle^* \quad (2.15)$$

where the RHS cancels to zero as shown by Ni and Beckermann [1991]. Moreover, the authors show that with their averaging technique, interfacial exchanges for energy, chemical species and momentum cancel out as they are equal in absolute value but opposite in sign. Regarding the LHS terms, their sum is defined along other variables as follows:

$$\langle \rho \rangle = g^l \langle \rho \rangle^l + g^s \langle \rho \rangle^s \quad (2.16)$$

$$\langle \rho \mathbf{v} \rangle = g^l \langle \rho \rangle^l \mathbf{v}^l + \cancel{g^s \langle \rho \rangle^s \mathbf{v}^s} \quad (2.17)$$

$$\langle \rho h \rangle = g^l \langle \rho \rangle^l \langle h \rangle^l + g^s \langle \rho \rangle^s \langle h \rangle^s \quad (2.18)$$

$$\langle \rho h \mathbf{v} \rangle = g^l \langle \rho \rangle^l \langle h \rangle^l \mathbf{v}^l + \cancel{g^s \langle \rho \rangle^s \langle h \rangle^s \mathbf{v}^s} \quad (2.19)$$

$$\langle \rho w_i \rangle = g^l \langle \rho \rangle^l w_i^l + g^s \langle \rho \rangle^s w_i^s \quad (2.20)$$

$$\langle \rho w_i \mathbf{v} \rangle = g^l \langle \rho \rangle^l w_i^l \mathbf{v}^l + \cancel{g^s \langle \rho \rangle^s w_i^s \mathbf{v}^s} \quad (2.21)$$

$$\left\langle \langle \rho \rangle^l \mathbf{v}^l \right\rangle = \left\langle \langle \rho \rangle^l \mathbf{v}^l \right\rangle^l = g^l \langle \rho \rangle^l \mathbf{v}^l \quad (2.22)$$

$$\left\langle \langle \rho \rangle^l \mathbf{v}^l \times \mathbf{v} \right\rangle = g^l \langle \rho \rangle^l \mathbf{v}^l \times \mathbf{v}^l + \cancel{g^s \langle \rho \rangle^s \mathbf{v}^l \times \mathbf{v}^s} \quad (2.23)$$

The average diffusive fluxes $j_{\psi\phi}$, represented by q for energy and j_i for each solute species. They are respectively modelled using Fourier's thermal conduction law and Fick's first mass diffusion law:

$$\langle q \rangle = -g^l \langle \kappa \rangle^l \nabla T - g^s \langle \kappa \rangle^s \nabla T = -\langle \kappa \rangle \nabla T \quad (2.24)$$

$$\langle j_i \rangle = -g^l \langle \rho \rangle^l D^l \nabla w_i^l - \cancel{g^s \langle \rho \rangle^s D^s \nabla w_i^s} \quad (2.25)$$

In eq. (2.25), the macroscopic diffusion coefficient in the solid is neglected, by considering that for macroscopic scales, the average composition of the alloy is much more influenced by advective and diffusive transport in the liquid. In eq. (2.24), we assume that phases are at thermal equilibrium, that is, temperature is uniform in the RVE.

Using eqs. (2.16) to (2.25) and following the same procedure done in eq. (2.15), the averaged mass balance hence writes:

$$\frac{\partial \langle \rho \rangle}{\partial t} + \nabla \cdot \langle \rho \mathbf{v} \rangle = 0 \quad (2.26)$$

whereas the averaged energy balance writes:

$$\frac{\partial \langle \rho h \rangle}{\partial t} + \nabla \cdot \langle \rho h \mathbf{v} \rangle - \nabla \cdot (\langle \kappa \rangle \nabla T) = 0 \quad (2.27)$$

and finally the species balance writes:

$$\frac{\partial \langle \rho w_i \rangle}{\partial t} + \nabla \cdot \langle \rho w_i \mathbf{v} \rangle - \nabla \cdot \left(g^l \langle \rho \rangle^l D^l \nabla w_i^l \right) = 0 \quad (2.28)$$

As stated previously, the momentum balance in the solid phase is not taken into consideration, hence we do not sum the corresponding local conservation equations. This has consequences on the advection terms in energy and species conservation, and later on we will show the consequences on the momentum conservation in the liquid.

First, the advection terms in [eqs. \(2.27\)](#) and [\(2.28\)](#) shall be redefined by considering that the fluid is incompressible ($\nabla \cdot \langle \mathbf{v}^l \rangle = 0$), which yields:

$$\nabla \cdot \langle \rho h \mathbf{v} \rangle = \langle \mathbf{v}^l \rangle \cdot \nabla \left(\langle \rho \rangle^l \langle h \rangle^l \right) \quad (2.29)$$

$$\nabla \cdot \langle \rho w_i \mathbf{v} \rangle = \langle \mathbf{v}^l \rangle \cdot \nabla \left(\langle \rho \rangle^l w_i^l \right) \quad (2.30)$$

As for the liquid momentum balance, we write:

$$\frac{\partial}{\partial t} \left(\langle \rho \rangle^l g^l \mathbf{v}^l \right) + \nabla \cdot \left(\langle \rho \rangle^l g^l \mathbf{v}^l \times \mathbf{v}^l \right) = \nabla \cdot \left(g^l \overline{\overline{\boldsymbol{\sigma}^l}} \right) + g^l \mathbf{F}_v^l + \boldsymbol{\Gamma}^l \quad (2.31)$$

where \mathbf{F}_v^l is the vector of external body forces exerted on the liquid phase. In our case, it accounts for the fluid's weight:

$$\mathbf{F}_v^l = \langle \rho \rangle^l \mathbf{g} \quad (2.32)$$

The interfacial momentum transfer between the solid and liquid phases in [eq. \(2.31\)](#) is modelled by a momentum flux vector $\boldsymbol{\Gamma}^l$, consisting of hydrostatic and deviatoric

parts, such that:

$$\mathbf{\Gamma}^l = \mathbf{\Gamma}_p^l + \mathbf{\Gamma}_s^l \quad (2.33)$$

$$\mathbf{\Gamma}_p^l = p^{l*} \nabla g^l = p^l \nabla g^l \quad (2.34)$$

$$\mathbf{\Gamma}_s^l = -g^{l^2} \mu^l \mathbb{K}^{-1} (\mathbf{v}^l - \mathbf{v}^s) \quad (2.35)$$

where p^{l*} is the pressure at the interface, considered to be equal to the liquid hydrostatic pressure p^l , \mathbb{K} is a permeability scalar (isotropic) computed using [eq. \(1.2\)](#) and μ^l is the liquid's dynamic viscosity. The general form of the Cauchy liquid stress tensor in [eq. \(2.31\)](#) is decomposed as follows:

$$\langle \overline{\overline{\boldsymbol{\sigma}^l}} \rangle = g^l \overline{\overline{\boldsymbol{\sigma}^l}} = - \left(\langle p^l \rangle - \lambda \nabla \cdot \langle \mathbf{v}^l \rangle \right) \bar{\mathbf{I}} + \langle \overline{\overline{\mathbf{S}^l}} \rangle \quad (2.36)$$

where λ is a dilatational viscosity [[Dantzig and Rappaz 2009](#)] and $\overline{\overline{\mathbf{S}^l}}$ is the liquid strain deviator tensor.

In the literature, the coefficient λ is taken proportional to the viscosity: $\lambda = \frac{2}{3} \mu^l$. However, as we consider an incompressible flow, the divergence term vanishes, thus rewriting [eq. \(2.36\)](#) as follows:

$$\langle \overline{\overline{\boldsymbol{\sigma}^l}} \rangle = - \langle p^l \rangle \bar{\mathbf{I}} + \langle \overline{\overline{\mathbf{S}^l}} \rangle \quad (2.37a)$$

$$\langle \overline{\overline{\boldsymbol{\sigma}^l}} \rangle = - \langle p^l \rangle \bar{\mathbf{I}} + 2\mu^l \langle \overline{\overline{\boldsymbol{\epsilon}^l}} \rangle \quad (2.37b)$$

where the transition from [eq. \(2.37a\)](#) to [eq. \(2.37b\)](#) is made possible by assuming a Newtonian behaviour for the liquid phase. The strain rate tensor, $\langle \overline{\overline{\boldsymbol{\epsilon}^l}} \rangle$, depends on the average liquid velocity:

$$\langle \overline{\overline{\boldsymbol{\epsilon}^l}} \rangle = \frac{1}{2} \left(\overline{\nabla} \langle \mathbf{v}^l \rangle + \overline{\nabla}^t \langle \mathbf{v}^l \rangle \right) \quad (2.38)$$

Finally, we obtain the final form of momentum conservation in the liquid phase coupled with the averaged mass balance, by injecting [eqs. \(2.32\), \(2.34\), \(2.35\), \(2.37b\)](#)

and (2.38) in eq. (2.31):

$$\begin{aligned} \frac{\partial}{\partial t} \left(\langle \rho \rangle^l \langle \mathbf{v}^l \rangle \right) + \frac{1}{g^l} \nabla \cdot \left(\langle \rho \rangle^l \langle \mathbf{v}^l \rangle \times \langle \mathbf{v}^l \rangle \right) = \\ - g^l \nabla p^l - 2\mu^l \nabla \cdot \left(\overline{\nabla} \langle \mathbf{v}^l \rangle + \overline{\nabla}^t \langle \mathbf{v}^l \rangle \right) - g^l \mu^l \mathbb{K}^{-1} \langle \mathbf{v}^l \rangle + g^l \langle \rho \rangle^l \mathbf{g} \end{aligned} \quad (2.39)$$

where we intentionally employed the *superficial velocity*, $\langle \mathbf{v}^l \rangle = g^l \mathbf{v}^l$, as the main unknown, together with the liquid pressure p^l . This system, when modelled in 3D, has a total of 4 unknowns (velocity vector and pressure) and 3 equations (X, Y and Z projections for the velocity vector). A fourth equation provided by the mass balance (eq. (2.26)) is therefore added for closure, giving the following system of equations :

$$\begin{cases} \frac{\partial}{\partial t} \left(\langle \rho \rangle^l \langle \mathbf{v}^l \rangle \right) + \frac{1}{g^l} \nabla \cdot \left(\langle \rho \rangle^l \langle \mathbf{v}^l \rangle \times \langle \mathbf{v}^l \rangle \right) = \\ - g^l \nabla p^l - 2\mu^l \nabla \cdot \left(\overline{\nabla} \langle \mathbf{v}^l \rangle + \overline{\nabla}^t \langle \mathbf{v}^l \rangle \right) - g^l \mu^l \mathbb{K}^{-1} \langle \mathbf{v}^l \rangle + g^l \langle \rho \rangle^l \mathbf{g} \\ \nabla \cdot \langle \mathbf{v}^l \rangle = 0 \end{cases} \quad (2.40)$$

Last, the Boussinesq approximation allows taking a constant density in the inertial terms of eq. (2.40) while the variations responsible for buoyancy forces can be deduced from temperature and liquid concentration using thermodynamic databases or directly using known thermal and solutal expansion coefficients, respectively β_T and $\beta_{w_i^l}$, and the reference density value ρ_0^l :

$$\langle \rho \rangle^l = \rho_0^l \left(1 - \beta_T (T - T_0) - \sum_i \beta_{w_i^l} (w_i^l - \langle w_i \rangle_0^l) \right) \quad (2.41)$$

Hence, the final set of equations is better known as the incompressible *Navier-Stokes* equations, applied to a solidifying melt:

$$\begin{cases} \rho_0^l \left(\frac{\partial \langle \mathbf{v}^l \rangle}{\partial t} + \frac{1}{g^l} \nabla \cdot \left(\langle \mathbf{v}^l \rangle \times \langle \mathbf{v}^l \rangle \right) \right) = \\ - g^l \nabla p^l - 2\mu^l \nabla \cdot \left(\overline{\nabla} \langle \mathbf{v}^l \rangle + \overline{\nabla}^t \langle \mathbf{v}^l \rangle \right) - g^l \mu^l \mathbb{K}^{-1} \langle \mathbf{v}^l \rangle + g^l \langle \rho \rangle^l \mathbf{g} \\ \nabla \cdot \langle \mathbf{v}^l \rangle = 0 \end{cases} \quad (2.42)$$

Since all conservation equations were presented and simplified by the main assumption of a static solid phase, we may include them in a graphical summary in [sec-](#)

2.2 Eulerian and Lagrangian motion description

2.2.1 Overview

In mechanics, it is possible to describe motion using two well-known motion description: Eulerian and Lagrangian descriptions. To start with the latter, it describes the motion of a particle by attributing a reference frame that moves with the particle. In other words, the particle itself is the center of a reference frame moving at the same speed during time. The position vector, denoted by \mathbf{x} , is hence updated as follows:

$$\mathbf{x}^{(t+1)} = \mathbf{x}^{(t)} + \mathbf{v}\Delta t \quad (2.46)$$

As such, the total variation of any physical quantity ψ related to the particle can be found by deriving with respect to time, $\frac{d\psi}{dt}$. In contrast to the Lagrangian description, the Eulerian description considers a fixed reference frame and independent of the particle's trajectory. The total variation of ψ cannot be simply described by a temporal derivative, since the particle's velocity is not known to the reference frame, and thus the velocity effect, namely the advective transport of ψ , should also be considered as follows:

$$\frac{d\psi}{dt} = \frac{\partial\psi}{\partial t} + \underbrace{\mathbf{v} \cdot \nabla\psi}_{\text{Advective Transport}} \quad (2.47)$$

In this case, the LHS term is also known as *total* or *material derivative*. The importance of these motion descriptions is essential to solve mechanics, whether for fluids or solids, using a numerical method like the finite element method (FEM). One of the main steps of this method is to spatially discretise a continuum into a grid of points (nodes, vertices ...), where any physical field shall be accordingly discretised. Now, if we focus on a node where velocity has a non zero value and following the previously made analysis, two outcomes are possible: either the node would be fixed (Eulerian) or it would move by a distance proportional to the prescribed velocity (Lagrangian). In the latter case, points located on the boundaries constantly require an update of the imposed boundary conditions.

From these explanations, one can deduce that an Eulerian framework is suited for fluid mechanics problems where velocities are high and may distort the mesh points, whereas the Lagrangian framework is better suited for solid mechanics problems

2.2. Eulerian and Lagrangian motion description

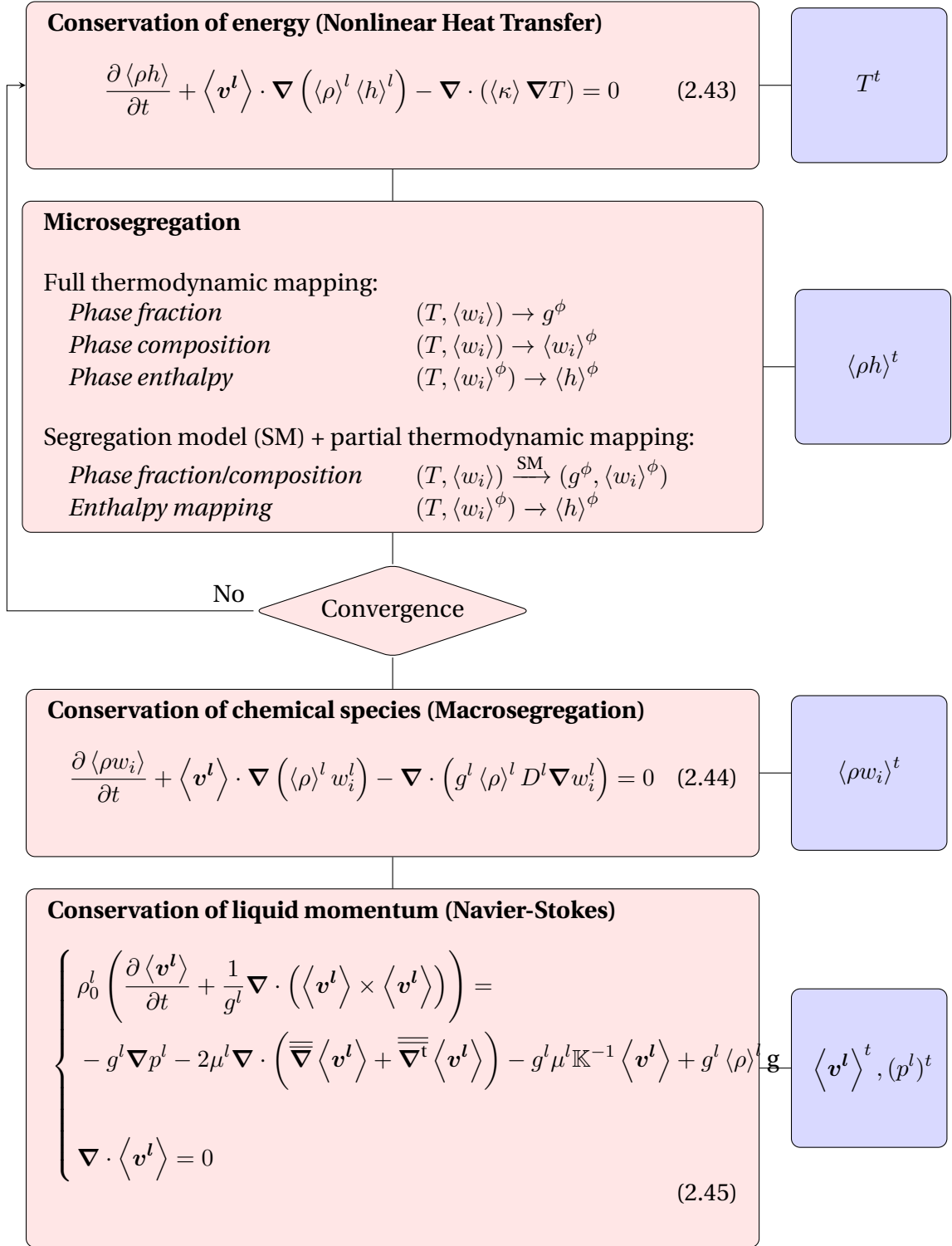


Fig. 2.1 – Graphical resolution algorithm of the conservation equations used in a monodomain macroscopic model to predict macrosegregation for a time increment t . The blue boxes represent the output of each equation.

where deformation velocities are relatively low and should well behave when predicting strains.

Another motion description has emerged some decades ago, [Hirt \[1971\]](#) call it the Arbitrary Lagrangian-Eulerian (ALE) method. ALE combines advantages from both previous descriptions as it dictates a Lagrangian behaviour at "solid" nodes where solid is deforming, and an Eulerian behaviour at "fluid" nodes.

2.2.2 Interface capturing

As no solid deformation is considered in this work, the Eulerian framework is a convenient choice. Solidification shrinkage is to be considered in our current scope, so it will deform the alloy's outer surface in contact with the air. We intend to track this interface and its motion over time via a numerical method. A wide variety of methods accomplish this task while they yield different advantages and disadvantages.

Such methods fall into two main classes, either interface tracking or interface capturing, among which we cite: marker-and-cell (MAC) [[Harlow and Welch 1965](#)], volume of fluid (VOF) [[Hirt and Nichols 1981](#)], phase field methods (PF), level set method (LSM) [[Osher and Sethian 1988](#)], coupled level set - VOF method and others. The interested reader may refer to quick references by [Prosperetti \[2002\]](#) and [Maitre \[2006\]](#) about these methods.

In the past years, the level set method received a considerable attention in many computational fields, specifically in solidification. For this reason, we will focus on this method henceforth, giving a brief literature review and technical details in the next sections.

2.3 Solidification models with level set

In classic solidification problems, the need to track an interface occurs usually at the solid-liquid interface, that is why the phase field method [[Karma and Rappel 1996](#); [Boettinger et al. 2002](#)] and the level set method [[Chen et al. 1997](#); [Gibou et al. 2003](#); [Tan and Zabaras 2007](#)] were applied at a microscale to follow mainly the dendritic growth of a single crystal in an undercooled melt. In our case however, when we mention "solidification models using LSM", we do not mean the solid-liquid interface inside the alloy, but it is the alloy(liquid)-air interface that we intend to track, assuming that microscale phenomena between the phases within the alloy, are averaged using the previously defined technique in [section 2.1.1](#).

Very few models were found in the literature, combining solidification and level set

as stated previously. Du et al. [2001] applied it to track the interface between two molten alloys in a double casting technique. Welding research, on another hand, has been more active adapting the level set methodology to corresponding applications. In CEMEF, two projects made use of the metal-air level set methodology in welding simulations and showed promising results. Desmaison et al. [2014] employed this methodology to simulate a hybrid arc and laser beam welding used in high thickness steel sheet welding. Later, Chen [2014] applied it to gas metal arc welding (GMAW) to predict the grain structure in the heat affected zone essentially. More recently, Courtois et al. [2014] used the same methodology but this time to predict keyhole defect formation in spot laser welding. The tracked interface in this case was that between the molten alloy and the corresponding vapor phase.

2.4 The level set method

Firstly introduced by Osher and Sethian [1988], this method became very popular in studying multiphase flows. It is reminded that the term *multiphase* in computational domains usually refers to multiple fluids, and thus should not be mixed with definition of a phase in the current solidification context. For disambiguation, we shall use *multifluid flow* when needed.

The great advantage lies in the way the interface between two fluids, F_1 and F_2 is implicitly captured, unlike other methods where the exact interface position is needed. In a discrete domain, the concept is to assign for each mesh node of position vector \mathbf{x} , the minimum distance $d_\Gamma(\mathbf{x})$ separating it from an interface Γ . The distance function, denoted α and defined in eq. (2.48), is then signed positive or negative, based on the fluid or domain to which the node belongs.

$$\alpha(\mathbf{x}) = \begin{cases} d_\Gamma(\mathbf{x}) & \text{if } \mathbf{x} \in F_1 \\ -d_\Gamma(\mathbf{x}) & \text{if } \mathbf{x} \in F_2 \\ 0 & \text{if } \mathbf{x} \in \Gamma_{F_1, F_2} \end{cases} \quad (2.48)$$

2.4.1 Diffuse interface

The level set has many attractive properties that allows seamless implementation in 2D and 3D models. It is a continuously differentiable C^1 -function. The Heaviside function is also continuous but non differentiable, with an abrupt transition from 0 to

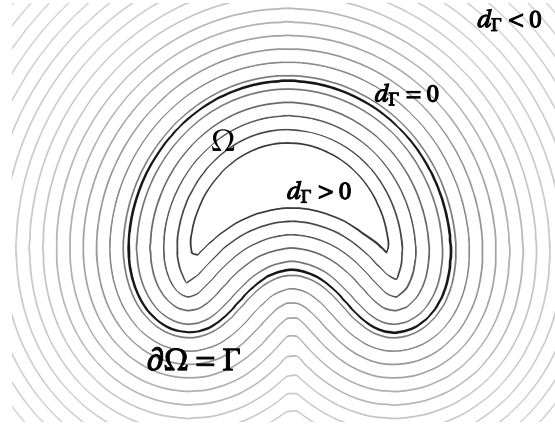


Fig. 2.2 – Schematic of the interface Γ (thick black line) of a rising air bubble (Ω) in water. The other contours represent isovalues of the distance function around and inside the interface contour. Those outside are signed negative whereas inside they are signed positive.

1 across the sharp interface, as follows:

$$H = H(\alpha(\mathbf{x})) = \begin{cases} 0 & \text{if } \alpha(\mathbf{x}) < 0 \\ 1 & \text{if } \alpha(\mathbf{x}) \geq 0 \end{cases} \quad (2.49)$$

With the help of [eq. \(2.49\)](#), we can define the geometric "presence" of a domain with respect to the interface. As such, material properties depend upon this function, which will be discussed later in [section 2.4.2](#). It is established that a steep transition can lead to numerical problems, so the Heaviside function should be smoothed in a volume of fixed thickness around the interface.

Sinusoidal smoothing in [eq. \(2.50\)](#) is widely used with level set formulations.

$$H = \begin{cases} 0 & \text{if } \alpha(\mathbf{x}) < -\varepsilon \\ 1 & \text{if } \alpha(\mathbf{x}) > \varepsilon \\ \frac{1}{2} \left(1 + \frac{\alpha(\mathbf{x})}{\varepsilon} + \frac{1}{\pi} \sin \left(\frac{\pi \alpha(\mathbf{x})}{\varepsilon} \right) \right) & \text{if } -\varepsilon \leq \alpha(\mathbf{x}) \leq \varepsilon \end{cases} \quad (2.50)$$

where the interval $[-\varepsilon; +\varepsilon]$ is an artificial interface thickness around the zero distance. Defining a diffuse interface rather than a sharp one, is also a common approach in phase field methods [[Beckermann et al. 1999](#); [Sun and Beckermann 2004](#)]. It is emphasized that the latter methods give physically meaningful analysis of a diffuse interface and the optimal thickness by thoroughly studying the intricate phenomena happening at the scale of the interface. However, for level set methods, there has not been a formal work leading the same type of analysis. For this reason, many aspects of the level set method lack physical meanings but remain computationally useful. In a recent

paper by [Gada and Sharma \[2009\]](#), the authors respond partially to this problem by analysing and deriving conservation equations using a level set in a more meaningful way, but do not discuss the diffuse interface aspect.

The Dirac delta function is also an important property to convert surface integrals to volume terms, which could turn useful when modelling surface tension effects for instance, using the *continuum surface force* method (CSF) [\[Brackbill et al. 1992\]](#). The Dirac function, plotted in [fig. 2.3](#) along with the Heaviside function within an interface thickness of $[-\varepsilon; +\varepsilon]$, is derived from the Heaviside as follows:

$$\delta(\alpha) = \delta(\alpha(\mathbf{x})) = \frac{\partial H}{\partial \alpha(\mathbf{x})} = \begin{cases} \frac{1}{2\varepsilon} \left(1 + \cos\left(\frac{\pi\alpha(\mathbf{x})}{\varepsilon}\right) \right) & \text{if } |\alpha(\mathbf{x})| \leq \varepsilon \\ 0 & \text{if } |\alpha(\mathbf{x})| > \varepsilon \end{cases} \quad (2.51)$$

The Heaviside and delta Dirac functions can be readily processed to obtain other geometric properties from the level set, which are extremely useful. We mention the most relevant ones [\[Peng et al. 1999\]](#):

$$\text{normal vector : } \mathbf{n} = \frac{\nabla \alpha}{\|\nabla \alpha\|} \quad (2.52)$$

$$\text{curvature : } \zeta = -\nabla \cdot \mathbf{n} \quad (2.53)$$

$$\text{surface area of the air-metal interface : } A^\Gamma = \int_{\Omega} \delta(\alpha) \|\nabla \alpha\| \, d\Omega \quad (2.54)$$

$$\text{metal volume : } V^M = \int_{\Omega} H^M \, d\Omega \quad (2.55)$$

where, for the last two equations, we consider a three-dimensional domain Ω containing two subdomains, metal and air, separated by an interface Γ . It is reminded that for a 2D case, [eq. \(2.54\)](#) evaluates a length instead of the area while [eq. \(2.55\)](#) gives the area instead of volume. Finally, within the diffuse interface, fluids properties may vary linearly or not, depending on the mixing law, which is presented in the next section.

2.4.2 Mixing Laws

A *monolithic* resolution style, as opposed to a *partitioned* resolution, is based on solving a single set of equations for both fluids separated by an interface, as if a single fluid were considered. Level set is one among many methods that use the monolithic style to derive a single set of conservation equations for both fluids. The switch from one material to the other is implicitly taken care of by using the Heaviside function as well as mixing laws. These laws are crucial to define how properties vary across the diffuse interface in view of a more accurate resolution. The most frequently used

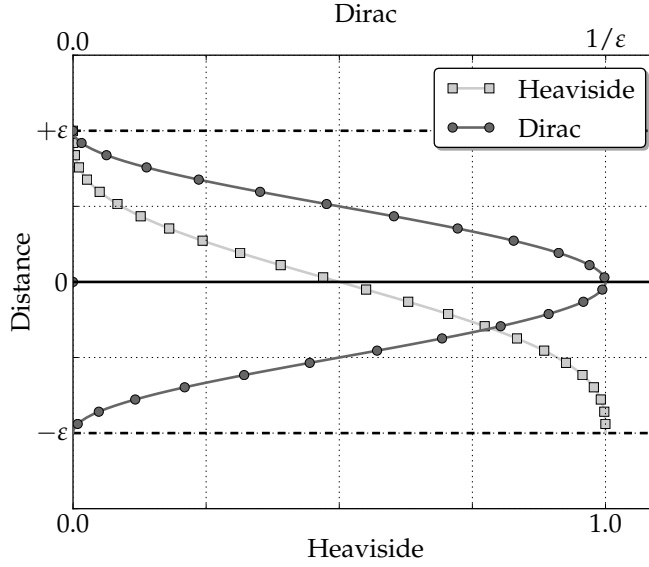


Fig. 2.3 – Schematic of two level properties inside the diffuse interface: Heaviside (lower x-axis) and Dirac delta (upper x-axis) functions. Note that the peak of the Dirac function depends on the interface thickness to ensure a unity integral of the delta function over Ω .

mixing law in the literature is the arithmetic law. Other transitions are less known such as the harmonic and logarithmic mixing. The first law is maybe the most intuitive and most used for properties mixture as it emanates from VOF-based methods. If we consider any property ψ (for instance the fluid's dynamic viscosity μ) then the arithmetic law will give a mixed property $\hat{\psi}$ as follows:

$$\hat{\psi} = H^{F_1} \psi^{F_1} + H^{F_2} \psi^{F_2} \quad (2.56)$$

Basically, the result is an average property that follows the same trend as the Heaviside function. As for the harmonic law, it writes:

$$\hat{\psi} = \left(\frac{H^{F_1}}{\psi^{F_1}} + \frac{H^{F_2}}{\psi^{F_2}} \right)^{-1} \quad (2.57)$$

and last, the logarithmic law writes:

$$\hat{\psi} = n^{(H^{F_1} \log_n \psi^{F_1} + H^{F_2} \log_n \psi^{F_2})} \quad (2.58)$$

where n is any real number serving as a logarithm base, which often is either the exponential e or 10. The mixture result with this law is the same, regardless of the value of n . By looking to [fig. 2.4](#), we clearly see that the difference between all three approaches is the property weight given to each side of the level set in the mixture. The

arithmetic law, being symmetric, has equal weights, ψ^{F_1} and ψ^{F_2} , in the final mixture. Nevertheless, the asymmetric harmonic mixing varies inside the diffuse interface with a dominant weight of one property over the other. As for the logarithmic mixture, it can be seen as an intermediate transition between the preceding laws. As long

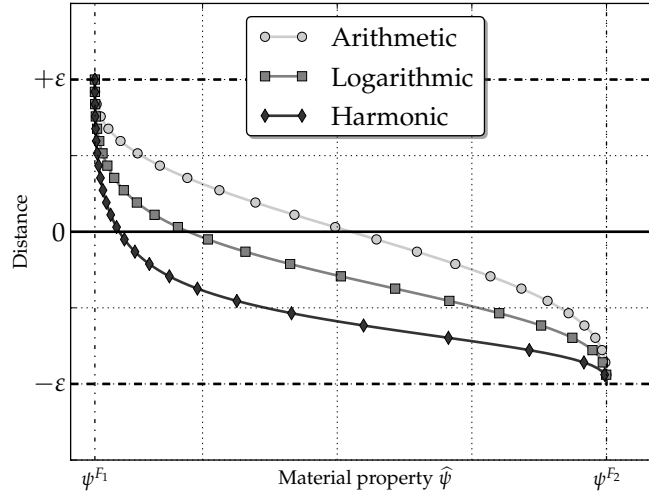


Fig. 2.4 – Three mixing laws, arithmetic, logarithmic and harmonic commonly used in monolithic formulations.

as the interface thickness is small enough, the choice of a mixing law should not drastically change the result, inasmuch as it depends on the discretisation resolution of the interface. This fact made the arithmetic mixing the most applied one, because it is symmetric and easy to implement (no handling of potential division problems like harmonic laws for instance). However, [Stroto et al. \[2008\]](#) claim that the harmonic law proves to conserve better diffusive fluxes at the interface. More recently, an interesting study made by [Ettrich et al. \[2014\]](#) focused on mixing thermal properties using a phase field method. They define a diffuse interface in which they separately mix the thermal conductivity, κ , and the heat capacity, C_p , then compute the thermal diffusivity as the ratio of these properties. Later, the authors compare the temperature field obtained by diffusion to a reference case in order to decide which combination of mixing laws gives the best result. Despite not being directly related to a level set method, this work gives an insight of the mixture possibilities and their effect on a pure thermal diffusion. Otherwise, little work has been found in the literature on the broad effects of mixture types on simulation results in a level set context.

2.5 Interface motion

When a physical interface needs to have topology changes because of fluid structure interaction or surface tension for instance, the level set model can follow these changes by a transport step. The idea is to advect the signed distance function, its zero isovalue representing the interface and all other distant isovalues, with the velocity field as input. The motion of the interface is thus expressed by:

$$\frac{d\alpha}{dt} = \frac{\partial\alpha}{\partial t} + \mathbf{v} \cdot \nabla\alpha = 0 \quad (2.59)$$

2.5.1 Level set transport

The finite element method gives the fully discretised weak form of [eq. \(2.59\)](#) by using a convenient set of test functions α^* belonging the Hilbertian *Sobolev* space:

$$\int_{\Omega} \alpha^* \frac{\partial\alpha}{\partial t} d\Omega + \int_{\Omega} \alpha^* \mathbf{v} \cdot \nabla\alpha d\Omega = 0 \quad \forall \alpha^* \in \mathcal{H}^1(\Omega) \quad (2.60)$$

The spatial discretisation of α assigns, for each of the total N nodes of a simplex, the following values:

$$\alpha = \sum_N P_j \alpha_j \quad (2.61)$$

Furthermore, with the standard Galerkin method, we replace test functions by the interpolation functions P_j , then we apply a temporal discretisation for the main unknowns by a forward (implicit) finite difference in time. Consequently, [eq. \(2.60\)](#) can be recast as follows:

$i, j : 1 \rightarrow \text{Nnodes}$

$$\frac{1}{\Delta t} (\alpha_j^t - \alpha_j^{t-\Delta t}) \int_{\Omega} P_i P_j d\Omega + \alpha_j^t \int_{\Omega} \mathbf{v}^t \cdot \nabla P_j d\Omega = 0 \quad (2.62a)$$

$$\left[\frac{1}{\Delta t} \int_{\Omega} P_i P_j d\Omega + \int_{\Omega} \mathbf{v}^t \cdot \nabla P_j d\Omega \right] \alpha_j^t = \frac{1}{\Delta t} \int_{\Omega} \alpha^{t-\Delta t} P_i d\Omega \quad (2.62b)$$

$$[\mathcal{M}_{ij} + \mathcal{A}_{ij}] \alpha_j^t = \mathcal{F}_i \quad (2.62c)$$

where \mathcal{M}_{ij} and \mathcal{A}_{ij} are respectively the mass (or capacity) matrix and advection matrix, both written within a local finite element, whereas \mathcal{F}_i is a local vector of known quantities from the previous time step. The solution of the linear system in [eq. \(2.62c\)](#) is the transported distance function.

When the convection regime becomes more dominant than diffusion (for high Reynolds number), the standard Galerkin method may lead to instabilities in the solution. In this case, stabilisation is crucial to avoid these oscillations, unless very fine remeshing is done "such that convection no longer dominates on an element level", as stated by Brooks and Hughes [1982]. The authors give a brief explanation of how numerically a convection-dominated equation can lead to oscillatory solutions with the standard Galerkin approximation. They proposed a stabilisation scheme, the Streamline Upwind Petrov-Galerkin, better known as SUPG, to stabilise advection dominated Navier-Stokes equations. However, their technique applies to any convection-diffusion equation. The SUPG method consists of modifying the test functions (like a classical Petrov-Galerkin method) by adding artificial diffusion in the flow direction. The modified test function writes:

$$\alpha_{SUPG}^* = \alpha^* + \underbrace{C_{SUPG}^E \left(\mathbf{v}_{\text{transport}} \cdot \nabla \alpha^* \right)}_{\text{Upwind contribution}} \quad (2.63)$$

where the upwind contribution for each finite element E depends on a stabilisation parameter C_{SUPG}^E that is expressed as follows:

$$C_{SUPG}^E = \frac{h^E}{v_{\text{flow}}^E} \quad (2.64)$$

Equation (2.64) shows that the SUPG parameter represents a time constant relative to an element mesh size, h^E , and an average velocity that should represent the magnitude in the flow direction. In the present work, all convection-diffusion equations are stabilised with the SUPG method, namely the conservation of mass, energy, momentum and chemical species as well as the level set transport.

2.5.2 Level set regularisation

Upon transport the distance function field, a crucial property of the level set may be partially or totally lost over the domain, which is:

$$\begin{cases} \|\nabla \alpha\| = 1 \\ \alpha(x, t) = 0 \end{cases} \quad \text{if } x \in \Gamma(t) \quad (2.65)$$

The closer this L^2 -norm to one, the more regular the level set. An irregular distance function induces cumulative numerical errors while transporting distance values far from the interface, resulting in wrong distance information, and loss of properties that

make up a "distance function". To show one the benefit of level set regularisation, [Basset \[2006\]](#) states after showing several tests of distance function transport, that regularised distance functions transported with a standard Galerkin method (i.e. without any stabilisation) show better "quality" globally in the domain, compared to initially non-regularised ones. When the transport equation in [eq. \(2.59\)](#) is discretised in time then solved, a *regularisation* (also known as *reinitialisation*) is necessary to conserve as much as possible the property in [eq. \(2.65\)](#).

[Figure 2.5](#) shows the need of regularisation in two different simulations of the same phenomenon: rising air bubble inside water. The importance of this well studied case [[Sussman et al. 1994](#); [Hysing et al. 2009](#)] is that the interface between two fluids is highly deformable as the bubble rises because of buoyancy, and therefore the task of tracking the dynamic interface while maintaining an accurate distance function is a considerable numerical task. In the first simulation, the distance contours are squeezed against the zero-distance contour marked by the thick black line. A closer look to the interface reveals undesired distortions, with a "wavy" shape at some points. This effect is evidently an artefact of a level set transport lacking subsequent reinitialisation, inasmuch as the surface tension tends to minimise the total surface area and make it as smooth as possible. Nevertheless, the second simulation unveils much better results, especially how the interface shows no sign of destabilisation. We also note the regular spacing between contours, which is a consequence of conserving the property defined in [eq. \(2.65\)](#). This improvement is attributed to the regularization done at each time step after the transport. In the forthcoming sections, we present three regularisation methods, then show their strong and weak points.

Classic Hamilton-Jacobi reinitialisation

In order to repair a distance function impaired by convective transport, [Sussman et al. \[1994\]](#) proposed solving a classic *Hamilton-Jacobi* equation, given in its most general form:

$$\frac{\partial \alpha}{\partial t} + \mathbb{H}(\alpha, x, t) = 0 \quad x \in \Omega, t > 0 \quad (2.66)$$

where $\alpha(x, t = 0) = \alpha_0$ is the initial value of the distance function. The term \mathbb{H} is known as the *Hamiltonian*. When the sign of the level set and its metric property ($\|\nabla \alpha\| = 1$) are considered, [eq. \(2.66\)](#) reduces to:

$$\frac{\partial \alpha}{\partial t} + S(\alpha) (\|\nabla \alpha\| - 1) = 0 \quad (2.67)$$

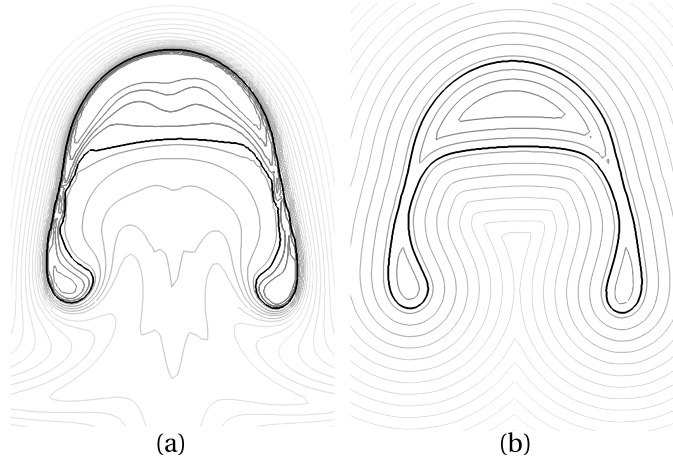


Fig. 2.5 – Schematic of the influence of level set regularisation on the distance function at the same time frame: a) without any regularisation step, the iso-value contours are distorted in the wake of the rising air bubble while being squeezed ahead of it, b) in contrast to regularising the distance function, where the contours maintain their spacing and geometric properties with respect to the tracked interface.

where $S(\alpha)$ is a step function giving the sign of the level set as follows:

$$S(\alpha) = \frac{\alpha}{|\alpha|} = \begin{cases} -1 & \text{if } \alpha < 0 \\ 0 & \text{if } \alpha = 0 \\ +1 & \text{if } \alpha > 0 \end{cases} \quad (2.68)$$

The sign function defined in [eq. \(2.68\)](#) is often smoothed to avoid numerical problems, as proposed for instance by [Sussman et al. \[1994\]](#):

$$S(\alpha) = S_\varepsilon(\alpha) = \frac{\alpha}{\sqrt{\alpha^2 + \varepsilon^2}} \quad (2.69)$$

where ε is a smoothing parameter that depends on the mesh size around the interface. However, one should be aware that within the smoothing thickness, the regularised function may suffer from local oscillations because of the reciprocal reinitialisation taking place at each side of the level set. [Peng et al. \[1999\]](#) states that this problem is more likely to happen if the initial level set shows very weak or very steep gradients, and therefore is not regular enough. The authors eventually propose a new sign function which would reinitialise the distance function, as close as possible to the interface without modifying the latter, as follows:

$$S(\alpha) = S_\varepsilon(\alpha) = \frac{\alpha}{\sqrt{\alpha^2 + \|\nabla \alpha\|^2 \varepsilon^2}} \quad (2.70)$$

Convective reinitialization

A recent work by [Ville et al. \[2011\]](#) introduced another concept for reinitialisation called the *convective reinitialisation*. The idea lies in combining both level set advection and regularisation in a single equation, saving resolution time. The key components of their method starts by defining a pseudo time step, $\Delta\tau$, that is linked to the main time variable through a numerical parameter λ_τ , as follows:

$$\lambda_\tau = \frac{\partial\tau}{\partial t} \quad (2.71)$$

The order of magnitude of λ_τ , which can be seen as a relaxation parameter [see [Vigneaux 2007](#), p. 89], is close to the ratio $h/\Delta t$. Then, the classic Hamilton-Jacobi [eq. \(2.66\)](#) is combined into the convection step by writing:

$$\frac{\partial\alpha}{\partial t} + (\mathbf{v} + \lambda_\tau \mathbf{U}) \cdot \nabla \alpha = \lambda_\tau S(\alpha) \quad (2.72)$$

where \mathbf{U} is a velocity vector in the normal direction to the interface, defined by $\mathbf{U} = S(\alpha)\mathbf{n}$, the normal vector \mathbf{n} being previously defined in [eq. \(2.52\)](#). The obvious shortcoming of convective reinitialisation is that it depends on a numerical parameter λ_τ . Another limitation of the method is the use of a sinusoidal filter to modify the distance function by truncating its values beyond a thickness threshold, which is also another parameter to calibrate the resolution. The drawback of truncating the level set is the loss of information far from the interface and the inability to fully reconstruct the distance function. If we denote this threshold by E and the modified level set by $\tilde{\alpha}$ inside the thickness, then [eq. \(2.72\)](#) is recast as:

$$\frac{\partial\alpha}{\partial t} + (\mathbf{v} + \lambda_\tau \mathbf{U}) \cdot \nabla \alpha = \lambda_\tau S(\alpha) \sqrt{1 - \left(\frac{\pi}{2E} \tilde{\alpha}\right)^2} \quad (2.73)$$

[Equation \(2.73\)](#) describes the transport and partial reconstruction of the distance function α , knowing its value $\tilde{\alpha}$ inside the thickness E .

Geometric reinitialization

This category of methods go from the level set's basic geometric principle to construct a distance function, instead of solving a partial differential system of equations as in the classic Hamilton-Jacobi reinitialisation. A widely known instance of this category is the *fast marching method* developed by [Sethian \[1996\]](#) and influenced by the [Dijkstra \[1959\]](#)'s method to compute the shortest path in a network of nodes. The method aims to solve the eikonal equation in [eq. \(2.65\)](#) to propagate the distance function in a single

direction by *upwinding*, i.e. going from low to high values of the distance function, while preserving a unitary distance gradient.

Direct reinitialisation is another interesting method in the geometric reinitialise category. However, it has not gained noticeable attention in the literature given the terrible cost in terms of computation time and efficiency if not optimised. The main idea is very simple: reconstruct the distance function over Ω as a subset of Ω , by computing the minimum distance between each mesh node and the interface. It means that, for any point $x \in \Omega$, the following constraint should be satisfied Osher and Fedkiw [2003]:

$$d_{\Gamma}(x) = \min \|x - x_{\Gamma}\| \quad \forall x_{\Gamma} \in \partial\Omega = \Gamma, \quad (2.74)$$

A efficient and optimised implementation of this method is done by Shakoor et al. [2015] making use of *k-d* trees to limit the search operations of elements and the subsequent distance evaluations in each of these elements. Moreover, the authors give a comparison of the previously stated methods on 2D and 3D cases, showing the great performance of direction reinitialisation when used with k-d trees algorithm, hence we use it in the present work.

2.6 Mesh adaptation

2.6.1 Metrics and anisotropy

The key to reduce spatial discretisation errors and obtain better results is a fine mesh. The optimal mesh resolution depends on the equations being discretised and solved on the FE grid, which consists of an array of structured triangles (fig. 2.6a), in the most basic situation. However, the potential of the Finite Element Method over other methods like the Finite Volume Method (FVM) is the use of unstructured grids. The easiest meshing solution one can choose is to create unstructured homogeneous and isotropic grid (fig. 2.6b), while respecting some constraints regarding the time step (temporal discretisation) stemming from physical or numerical conditions, e.g. diffusion shock constraint in diffusional transient equations or Courant–Friedrichs–Lewy (CFL) condition in transient advective equations. In such a case, errors due to interpolation are minimised, which guaranties good results but with expensive time cost.

Heterogeneous meshes (fig. 2.6c) that consist of fine isotropic elements in areas of interest along with coarser isotropic elements in other areas, may reduce the needed time to solver each conservation equation. Although this is an interesting alternative, it is less powerful than anisotropic meshing. In the latter (fig. 2.6d), elements adapt to a physical quantity, such as enthalpy or velocity, reducing the elemental length in the

direction where the gradient is higher, while stretching the element in the orthogonal direction. This allows more accurate resolution with less elements than needed by isotropic meshing. Moreover, this type of meshing is well adapted to the context of this thesis as it allows getting a fine mesh in the normal direction to the interface, that is in its transport direction, while reducing the number of elements in other directions. Regions undergoing solidification are also important to remesh since microsegregation starts in the mushy zone, i.e. between the liquidus and solidus temperatures given by a local average composition, where fluid flow may transport species, leading eventually to macrosegregation.

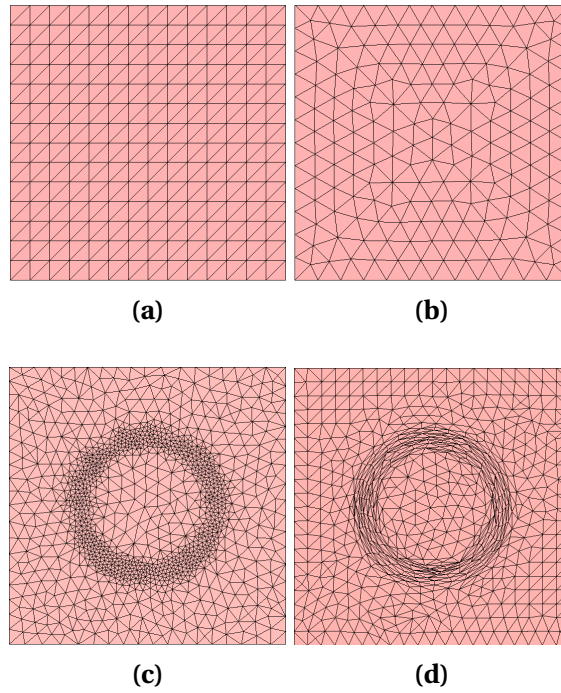


Fig. 2.6 – Alternatives for initial finite element grid generation: (a) structured homogeneous, (b) unstructured homogeneous isotropic, (c) unstructured heterogeneous isotropic and (d) unstructured heterogeneous anisotropic meshes.

Since mesh adaptation involves advanced mathematical notions, readers interested in the basics are referred to the following references: [Coupez 1991; Coupez 2000; Gruau and Coupez 2005; Jannoun 2014]. In this study, we show and compare different remeshing methods relevant to macrosegregation prediction, and based on previous work done at CEMEF. These techniques rely on metric tensors, and some of them belong to *a posteriori* error estimators category. A metric or a metric tensor \mathcal{M} , also known as *Riemannian* metric, is a positive symmetric definite matrix that relates to

an element's size in \mathbb{R}^3 via:

$$\mathcal{M} = \begin{pmatrix} M_{11} & M_{12} & M_{13} \\ M_{12} & M_{22} & M_{23} \\ M_{13} & M_{23} & M_{33} \end{pmatrix} = \mathcal{R} \begin{pmatrix} 1/h_x^2 & 0 & 0 \\ 0 & 1/h_y^2 & 0 \\ 0 & 0 & 1/h_z^2 \end{pmatrix} \mathcal{R}^T \quad (2.75)$$

where \mathcal{R} is a rotation matrix and h_x , h_y and h_z are the respective dilatation scalars defined by the metric in the (x, y, z) space, describing a three-dimensional anisotropy. The metric information is then passed to a mesh generation tool, called *MTC*, which is based on an iterative procedure of local topology optimisations. We focus hereafter on two adaptive remeshing techniques, then discuss the functional details and show some examples.

2.6.2 *Remesh2*: Interface remeshing

Remesh2 is an explicit method to compute an anisotropic metric around the zero surface of a distance function. The idea is, as mentioned previously, to reduce the elements cost in the tangential directions to level set by stretching the elements, leaving small element lengths in the normal direction, where the level set gradient is the greatest. This method is not based on error estimators, but rather on explicit input from the user who chooses the mesh size in normal and tangential directions to the interface, as well as in the positive and negative regions delimited by the level set. The following parameters are used as input data to determine the final node-wise metric:

h_n	mesh size in the normal direction of the level set
h_τ	mesh size in the tangential directions of the level set
h_M	mesh size in the metal
h_A	mesh size in the air
α	distance function (level set)
ε	level set mixing thickness
\mathbf{V}	arbitrary vector

Algorithm 1: *Remesh2* metric construction

Data: \mathbf{n} h_M h_A h_n h_τ α

Result: \mathcal{M}_2

Initialise node index: $j = 0$;

while $j \leq j_{end}$ **do**

if $\alpha_j < \varepsilon$ **then**

 Compute normal direction to level set: $\mathbf{n} = \nabla\alpha / \|\nabla\alpha\|$;

 Compute the first tangential direction: $\boldsymbol{\tau}_1 = \mathbf{V} - (\mathbf{V} \cdot \mathbf{n}) \cdot \mathbf{n}$;

 Deduce the second tangential direction: $\boldsymbol{\tau}_2 = \mathbf{n} \wedge \boldsymbol{\tau}_1$;

 Compute rotation matrix and its transpose: \mathcal{R}_j and \mathcal{R}_j^{-1} ;

 Deduce P1 metric at node j : $(\mathcal{M}_2)_j = \mathcal{R}_j \Lambda \mathcal{R}_j^{-1}$

else

 go back to the beginning of current section;

 Increment j ;

2.6.3 *Remesh4*: Multi-criteria remeshing

It is a metric construction method based on edge-based error distribution

What i concluded from Z-FAST-SMACS cases A and B, where remesh4 was used in two different ways (LS and velocity/100 , LS and ConcentrationPosNeg) is that for diffuse interface thickness less than 2e-4 m, mass conservation gets all sorts of problems, because of low element resolution around interface while higher resolution at the tips of the transition region

To do ?

Interface Remeshing: Importance when using a static level set and more importantly when LS is transported, influence of mixing area *thickness* and *resolution* (i.e. nb of nodes with the area), Isotropic or anisotropic ? the first is more important to composition calculation while the second is more relevant if we mean do thermohydraulics without macrosegregation

Résumé chapitre 2

Bibliography

[Basset 2006]

Basset, O. (2006). “Simulation numérique d’écoulements multi-fluides sur grille de calcul”. PhD Thesis. École Nationale Supérieure des Mines de Paris. URL: <https://tel.archives-ouvertes.fr/tel-00376484> (cited on page 38).

[Beckermann et al. 1999]

Beckermann, C., Diepers, H. J., Steinbach, I., Karma, A., and Tong, X (1999). “Modeling Melt Convection in Phase-Field Simulations of Solidification”. *Journal of Computational Physics*, 154 (2), pp. 468–496. URL: <http://www.sciencedirect.com/science/article/pii/S0021999199963234> (cited on page 32).

[Boettinger et al. 2002]

Boettinger, W. J., Warren, J. A., Beckermann, C., and Karma, A. (2002). “Phase-Field Simulation of Solidification1”. *Annual Review of Materials Research*, 32 (1), pp. 163–194. URL: <http://dx.doi.org/10.1146/annurev.matsci.32.101901.155803> (cited on page 30).

[Brackbill et al. 1992]

Brackbill, J. U., Kothe, D. B., and Zemach, C (1992). “A continuum method for modeling surface tension”. *Journal of Computational Physics*, 100 (2), pp. 335–354. URL: <http://www.sciencedirect.com/science/article/pii/002199919290240Y> (cited on page 33).

[Brooks and Hughes 1982]

Brooks, A. N. and Hughes, T. J. R. (1982). “Streamline upwind/Petrov-Galerkin formulations for convection dominated flows with particular emphasis on the incompressible Navier-Stokes equations”. *Computer Methods in Applied Mechanics and Engineering*, 32 (1–3), pp. 199–259. URL: <http://www.sciencedirect.com/science/article/pii/0045782582900718> (cited on page 37).

[Chen et al. 1997]

Chen, S., Merriman, B., Osher, S., and Smereka, P. (1997). “A Simple Level Set Method for Solving Stefan Problems”. *Journal of Computational Physics*, 135 (1), pp. 8–29. URL: <http://www.sciencedirect.com/science/article/pii/S0021999197957211> (cited on page 30).

[Chen 2014]

Chen, S. (2014). “Three dimensional Cellular Automaton - Finite Element (CAFE) modeling for the grain structures development in Gas Tungsten / Metal Arc Welding processes”. PhD Thesis. Ecole Nationale Supérieure des Mines de Paris. URL: <https://pastel.archives-ouvertes.fr/pastel-01038028> (cited on page 31).

Bibliography

[Clyne and Kurz 1981]

Clyne, T. W. and Kurz, W. (1981). "Solute redistribution during solidification with rapid solid state diffusion". *Metallurgical Transactions A*, 12 (6), pp. 965–971. URL: <http://link.springer.com/article/10.1007/BF02643477> (cited on page 21).

[Combeau et al. 1996]

Combeau, H., Drezet, J.-M., Mo, A., and Rappaz, M. (1996). "Modeling of microsegregation in macrosegregation computations". *Metallurgical and Materials Transactions A*, 27 (8), pp. 2314–2327. URL: <http://link.springer.com/article/10.1007/BF02651886> (cited on page 21).

[Coupez 1991]

Coupez, T. (1991). *Grandes transformations et remaillage automatique*. EMP. URL: <http://www.theses.fr/1991ENMP0615> (cited on page 42).

[Coupez 2000]

Coupez, T. (2000). "Génération de maillage et adaptation de maillage par optimisation locale". *Revue Européenne des Éléments*, 9 (4), pp. 403–423. URL: <http://www.tandfonline.com/doi/abs/10.1080/12506559.2000.10511454> (cited on page 42).

[Courtois et al. 2014]

Courtois, M., Carin, M., Masson, P. L., Gaied, S., and Balabane, M. (2014). "A complete model of keyhole and melt pool dynamics to analyze instabilities and collapse during laser welding". *Journal of Laser Applications*, 26 (4), p. 042001. URL: <http://scitation.aip.org/content/lia/journal/jla/26/4/10.2351/1.4886835> (cited on page 31).

[Dantzig and Rappaz 2009]

Dantzig, J. A. and Rappaz, M. (2009). *Solidification*. EPFL Press (cited on pages 21–23, 26).

[Desmaison et al. 2014]

Desmaison, O., Bellet, M., and Guillemot, G. (2014). "A level set approach for the simulation of the multipass hybrid laser/GMA welding process". *Computational Materials Science*, 91, pp. 240–250. URL: <http://www.sciencedirect.com/science/article/pii/S092702561400278X> (cited on page 31).

[Dijkstra 1959]

Dijkstra, E. W. (1959). "A note on two problems in connexion with graphs". *Numerische Mathematik*, 1 (1), pp. 269–271. URL: <http://link.springer.com/article/10.1007/BF01386390> (cited on page 40).

[Du et al. 2001]

Du, Q., Li, D., Li, Y., Li, R., and Zhang, P. (2001). "Simulating a double casting technique using level set method". *Computational Materials Science*, 22 (3–4), pp. 200–212. URL: <http://www.sciencedirect.com/science/article/pii/S0927025601001902> (cited on page 31).

[Ettrich et al. 2014]

Ettrich, J., Choudhury, A., Tschukin, O., Schoof, E., August, A., and Nestler, B. (2014). "Modelling of transient heat conduction with diffuse interface methods". *Modelling and Simulation in Materials Science and Engineering*, 22 (8), p. 085006. URL: <http://iopscience.iop.org/0965-0393/22/8/085006> (cited on page 35).

[Gada and Sharma 2009]

Gada, V. H. and Sharma, A. (2009). "On Derivation and Physical Interpretation of Level Set Method-Based Equations for Two-Phase Flow Simulations". *Numerical Heat Transfer, Part B: Fundamentals*, 56 (4), pp. 307–322. URL: <http://dx.doi.org/10.1080/10407790903388258> (cited on page 33).

[Gibou et al. 2003]

Gibou, F., Fedkiw, R., Caflisch, R., and Osher, S. (2003). "A Level Set Approach for the Numerical Simulation of Dendritic Growth". *Journal of Scientific Computing*, 19 (1-3), pp. 183–199. URL: <http://link.springer.com/article/10.1023/A:3A1025399807998> (cited on page 30).

[Gruau and Coupez 2005]

Gruau, C. and Coupez, T. (2005). "3D tetrahedral, unstructured and anisotropic mesh generation with adaptation to natural and multidomain metric". *Computer Methods in Applied Mechanics and Engineering*, Unstructured Mesh Generation 194 (48–49), pp. 4951–4976. URL: <http://www.sciencedirect.com/science/article/pii/S0045782505000745> (cited on page 42).

[Harlow and Welch 1965]

Harlow, F. H. and Welch, J. E. (1965). "Numerical Calculation of Time-Dependent Viscous Incompressible Flow of Fluid with Free Surface". *Physics of Fluids (1958-1988)*, 8 (12), pp. 2182–2189. URL: <http://scitation.aip.org/content/aip/journal/pof1/8/12/10.1063/1.1761178> (cited on page 30).

[Hirt 1971]

Hirt, C. W. (1971). "An arbitrary Lagrangian-Eulerian computing technique". *Proceedings of the Second International Conference on Numerical Methods in Fluid Dynamics*. Ed. by M. Holt. Lecture Notes in Physics 8. Springer Berlin Heidelberg, pp. 350–355. URL: http://link.springer.com/chapter/10.1007/3-540-05407-3_50 (cited on page 30).

[Hirt and Nichols 1981]

Hirt, C. W and Nichols, B. D (1981). "Volume of fluid (VOF) method for the dynamics of free boundaries". *Journal of Computational Physics*, 39 (1), pp. 201–225. URL: <http://www.sciencedirect.com/science/article/pii/0021999181901455> (cited on page 30).

[Hysing et al. 2009]

Hysing, S., Turek, S., Kuzmin, D., Parolini, N., Burman, E., Ganesan, S., and Tobiska, L. (2009). "Quantitative benchmark computations of two-dimensional bubble dynamics". *International Journal for Numerical Methods in Fluids*, 60 (11), pp. 1259–1288. URL: <http://onlinelibrary.wiley.com/doi/10.1002/flid.1934/abstract> (cited on page 38).

[Jannoun 2014]

Jannoun, G. E. (2014). "Space-Time accurate anisotropic adaptation and stabilized finite element methods for the resolution of unsteady CFD problems". PhD thesis. Ecole Nationale Supérieure des Mines de Paris. URL: <https://pastel.archives-ouvertes.fr/tel-01146245/document> (cited on page 42).

[Karma and Rappel 1996]

Karma, A. and Rappel, W.-J. (1996). "Phase-field method for computationally efficient modeling of solidification with arbitrary interface kinetics". *Physical Review E*, 53 (4), R3017–R3020. URL: <http://link.aps.org/doi/10.1103/PhysRevE.53.R3017> (cited on page 30).

Bibliography

[Khan et al. 2014]

Khan, M. I., Mostafa, A. O., Aljarrah, M., Essadiqi, E., and Medraj, M. (2014). “Influence of Cooling Rate on Microsegregation Behavior of Magnesium Alloys”. *Journal of Materials*, 2014, e657647. URL: <http://www.hindawi.com/journals/jma/2014/657647/abs/> (cited on page 21).

[Kobayashi 1988]

Kobayashi, S. (1988). “Solute redistribution during solidification with diffusion in solid phase: A theoretical analysis”. *Journal of Crystal Growth*, 88 (1), pp. 87–96. URL: <http://www.sciencedirect.com/science/article/pii/S0022024898900100> (cited on page 21).

[Maitre 2006]

Maitre, E. (2006). “Review of numerical methods for free interfaces”. Les Houches, France. URL: <http://goo.gl/Re6f3a> (cited on page 30).

[Martorano et al. 2003]

Martorano, M. A., Beckermann, C., and Gandin, C.-A. (2003). “A solutal interaction mechanism for the columnar-to-equiaxed transition in alloy solidification”. *Metallurgical and Materials Transactions A*, 34 (8), pp. 1657–1674. URL: <http://link.springer.com/article/10.1007/s11661-003-0311-x> (cited on page 21).

[Ni and Beckermann 1991]

Ni, J. and Beckermann, C. (1991). “A volume-averaged two-phase model for transport phenomena during solidification”. *Metallurgical Transactions B*, 22 (3), pp. 349–361. URL: <http://link.springer.com/article/10.1007/BF02651234> (cited on pages 21, 22, 24).

[Osher and Fedkiw 2003]

Osher, S. and Fedkiw, R. (2003). “Signed Distance Functions”. *Level Set Methods and Dynamic Implicit Surfaces*. Applied Mathematical Sciences 153. Springer New York, pp. 17–22. URL: http://link.springer.com/chapter/10.1007/0-387-22746-6_2 (cited on page 41).

[Osher and Sethian 1988]

Osher, S. and Sethian, J. A. (1988). “Fronts propagating with curvature-dependent speed: Algorithms based on Hamilton-Jacobi formulations”. *Journal of Computational Physics*, 79 (1), pp. 12–49. URL: <http://www.sciencedirect.com/science/article/pii/0021999188900022> (cited on pages 30, 31).

[Peng et al. 1999]

Peng, D., Merriman, B., Osher, S., Zhao, H., and Kang, M. (1999). “A PDE-Based Fast Local Level Set Method”. *Journal of Computational Physics*, 155 (2), pp. 410–438. URL: <http://www.sciencedirect.com/science/article/pii/S0021999199963453> (cited on pages 33, 39).

[Prosperetti 2002]

Prosperetti, A. (2002). “Navier-Stokes Numerical Algorithms for Free-Surface Flow Computations: An Overview”. *Drop-Surface Interactions*. Ed. by M. Rein. CISM International Centre for Mechanical Sciences 456. Springer Vienna, pp. 237–257. URL: http://link.springer.com/chapter/10.1007/978-3-7091-2594-6_8 (cited on page 30).

[Sethian 1996]

Sethian, J. A. (1996). “A fast marching level set method for monotonically advancing fronts”. *Proceedings of the National Academy of Sciences*, 93 (4), pp. 1591–1595. URL: <http://www.pnas.org/content/93/4/1591> (cited on page 40).

[Shakoor et al. 2015]

Shakoor, M., Scholtes, B., Bouchard, P.-O., and Bernacki, M. (2015). “An efficient and parallel level set reinitialization method - Application to micromechanics and microstructural evolutions”. *Applied Mathematical Modelling* (submitted), (cited on page 41).

[Strotos et al. 2008]

Strotos, G., Gavaises, M., Theodorakakos, A., and Bergeles, G. (2008). “Numerical investigation of the cooling effectiveness of a droplet impinging on a heated surface”. *International Journal of Heat and Mass Transfer*, 51 (19–20), pp. 4728–4742. URL: <http://www.sciencedirect.com/science/article/pii/S001793100800149X> (cited on page 35).

[Sun and Beckermann 2004]

Sun, Y. and Beckermann, C. (2004). “Diffuse interface modeling of two-phase flows based on averaging: mass and momentum equations”. *Physica D: Nonlinear Phenomena*, 198 (3–4), pp. 281–308. URL: <http://www.sciencedirect.com/science/article/pii/S0167278904003689> (cited on page 32).

[Sussman et al. 1994]

Sussman, M., Smereka, P., and Osher, S. (1994). “A Level Set Approach for Computing Solutions to Incompressible Two-Phase Flow”. *Journal of Computational Physics*, 114 (1), pp. 146–159. URL: <http://www.sciencedirect.com/science/article/pii/S0021999184711557> (cited on pages 38, 39).

[Tan and Zabaras 2007]

Tan, L. and Zabaras, N. (2007). “A level set simulation of dendritic solidification of multi-component alloys”. *Journal of Computational Physics*, 221 (1), pp. 9–40. URL: <http://www.sciencedirect.com/science/article/pii/S0021999106002737> (cited on page 30).

[Touret and Gandin 2009]

Touret, D. and Gandin, C. A. (2009). “A generalized segregation model for concurrent dendritic, peritectic and eutectic solidification”. *Acta Materialia*, 57 (7), pp. 2066–2079. URL: <http://www.sciencedirect.com/science/article/pii/S1359645409000184> (cited on page 21).

[Vigneaux 2007]

Vigneaux, P. (2007). “Méthodes Level Set pour des problèmes d’interface en microfluidique”. PhD thesis. Université Sciences et Technologies - Bordeaux I. URL: <https://tel.archives-ouvertes.fr/tel-00189409/document> (cited on page 40).

[Ville et al. 2011]

Ville, L., Silva, L., and Coupez, T. (2011). “Convected level set method for the numerical simulation of fluid buckling”. *International Journal for Numerical Methods in Fluids*, 66 (3), pp. 324–344. URL: <http://onlinelibrary.wiley.com/doi/10.1002/fld.2259/abstract> (cited on page 40).

[Wang and Beckermann 1993]

Wang, C. Y. and Beckermann, C. (1993). “A multiphase solute diffusion model for dendritic alloy solidification”. *Metallurgical Transactions A*, 24 (12), pp. 2787–2802. URL: <http://link.springer.com/article/10.1007/BF02659502> (cited on page 21).